Scripta Materialia 213 (2022) 114585

Contents lists available at ScienceDirect

Scripta Materialia

journal homepage: www.journals.elsevier.com/scripta-materialia

On the solid-state dendritic growth of M_7C_3 carbide at interfaces in an austenitic system

Yuanbo T. Tang [a,1,*], Anh Hoang Pham [b,c,1], Shigekazu Morito [b,c], D. Graham McCartney [a,c], Roger C. Reed [a,c]

[a] *Department of Materials, University of Oxford, Parks Road, Oxford OX1 3PH, United Kingdom*
[b] *Department of Physics and Materials Science, Shimane University, Matsue, Shimane 690-8504, Japan*
[c] *Next Generation Tatara Co-Creation Centre (NEXTA), Shimane University, Matsue, Shimane 690-8504, Japan*

ARTICLE INFO

Keywords:
Dendritic growth
In-situ characterisation
Alloy 600
Carbide
Confocal laser scanning microscope
FIB tomography
Cr-depletion
Stress corrosion cracking

ABSTRACT

Solid-state growth of M_7C_3 carbide at different interfaces in an austenitic Ni–Cr–Fe alloy (Alloy 600) was studied in-situ by high temperature confocal laser scanning microscopy during continuous cooling from 1140 °C. The carbide develops a dendritic morphology and grows laterally across the free surface via a diffusion-assisted mechanism. Primary dendrite arms can extend beyond 100 μm, with some dendrites also developing secondary arms with spacing approximately 3.0 μm. By using focused ion beam tomography, some of the surface carbides are found to be directly connected to dendritic carbide at grain boundaries in the bulk confirming they originated from the same nucleus. Matrix deformation is induced in the vicinity of a carbide during growth. This work provides significant insight into the important topic of carbide development by a rare combination of both in-situ microscopy and a 3D tomographic technique; the new knowledge discovered is expected to apply to other austenitic systems.

Austenitic alloys are widely used for components in power generation, such as pressurised and boiling water reactors (PWR/BWR) in the nuclear industry. Their insertion is justified by the excellent corrosion resistance, formability and mechanical integrity at extreme temperatures [1,2]. The typical microstructure in those alloys, such as stainless steels (316, 304) or else nickel alloys (Alloy 600, Alloy 690) consists of an austenite matrix with carbide decorating the matrix and/or the grain boundaries [3]. The long-term performance in service is strongly influenced by the carbide distribution, where most failures originate along grain boundaries facilitated by carbide in corrosive environments, e.g. stress corrosion cracking (SCC) [4,5]. As determined via high-resolution characterisation and micro-mechanical analysis [2], the crucial carbides needing careful control are intergranular Cr-rich $M_{23}C_6$ and M_7C_3 [6,7]. Those precipitates alter deformation characteristics via changing local microstructure and chemistry, i.e. Cr-depletion, and consequently accelerate the oxide growth that leads to embrittlement [8].

However, tailoring and design of carbide precipitation is not straightforward for various reasons. First, its phase transformation temperature is very sensitive to carbon content. For example, a small change of 0.03 wt.% of carbon can induce ~100 K change in carbide dissolution temperature [9]. It influences the effective heat treatment window and gives rise to inconsistency in welding repair [10]. Second, the carbide nucleation events and growth lack fundamental knowledge and direct evidence [11], understandably due to the technical difficulties of such experimentation. Third, thermal history is also important for carbide phase transformations as various distributions can be achieved for the same composition as a result of different thermal treatments [9,12]. Carbide morphology is frequently described as, for example, granular, faceted, film-like, script-like or needle-like. It is thus evident that, despite carbide growth occurring in three dimensions, the common morphological descriptors are applicable only to two-dimensional sections. Efforts in characterising the 3D morphology of carbides are therefore needed to shed light on their formation and potential role during corrosion, deformation and fracture.

The work reported in this paper was motivated by the above and its aim was to study carbide formation and evolution using a combination of in-situ high temperature confocal laser scanning microscopy (HT-CLSM) combined with an ex-situ characterisation by 3D focused ion

---

* Corresponding author.
E-mail address: yuanbo.tang@materials.ox.ac.uk (Y.T. Tang).
[1] These authors contributed equally.

https://doi.org/10.1016/j.scriptamat.2022.114585
Received 14 August 2021; Received in revised form 18 January 2022; Accepted 4 February 2022
Available online 13 February 2022
1359-6462/© 2022 The Authors. Published by Elsevier Ltd on behalf of Acta Materialia Inc. This is an open access article under the CC BY-NC-ND license (http://creativecommons.org/licenses/by-nc-nd/4.0/).

Table 1
Alloy composition used for current study in wt-% (Ni-base), measured using ICP-OES, ICP-combustion (carbon) and Spark OES (boron).

Ni	Cr	Fe	C	Co	B	Ti
bal	15.75	9.12	0.071	0.04	0.004	0.22

beam and scanning electron microscope (FIB-SEM) tomography. A typical nuclear reactor austenitic, nickel-based alloy (Alloy 600) with a Cr-rich carbide phase was investigated. The study had a specific focus on carbide growth upon cooling from the austenite phase from above the carbide solvus temperature. In-situ experiments were conducted to observe the precipitation reaction of carbide during continuous cooling and so to provide insight into the carbide nucleation and growth. Furthermore, the ex-situ 3D FIB tomography was implemented to reconstruct the morphology of carbides formed on the surface and at the grain boundaries in the bulk to obtain a better understanding than that gained from traditional planar 2D sections. The ex-situ studies were necessary to establish whether in-situ observations are truly representative of those occurring in the bulk.

The chemical composition of the Alloy 600 used in this study is shown in Table 1. An 8 mm diameter bar was solution annealed at 1140 °C for 2 h to dissolve any pre-existing carbide and then water quenched. Samples were cut and polished to a thickness of ≈ 350 μm with a colloidal silica finish. The in-situ observation of the microstructure was carried out using a HT-CLSM, model VL2000DX-SVF18SP (Yonekura Ltd, Japan). The sample was heated by thermal radiation from a 1.5 kW halogen lamp (see Figure S1 in supplementary information). To reduce the residual oxygen level and minimise carbon contamination during in-situ observations, three purging cycles were applied to eliminate residual gases before heating, each of which comprised three-minute evacuation by rotary vacuum pump and one-minute ultra-purity Ar (99.9999%) flow at 500 sccm (standard cubic centimetre per minute). After this purging cycle, ultra-high purity Ar gas flow was maintained at 200 sccm throughout the in-situ experiment. By applying these precautions, no evidence for surface contamination of the sample was found by scanning electron microscopy of the sample after completion of the thermal cycle. In addition, a customised oxygen getter ring (commercial purity Zr) was placed just above the sample surface, which successfully suppressed oxidation of Alloy 600 during the experiment. Figures S2–S4 in the supplementary information demonstrate that, without the application of the getter ring, there was severe oxidation of the sample surface. The sample temperature was calibrated up to 1180 °C by using a dummy sample with a spot-welded thermocouple. In this work the sample surface was observed in-situ through a quartz window using a 405 nm ultra-violet laser with a long-working distance lens and images were captured at the rate of 15 fps. The sample was heated from ambient temperature to 1140 °C at 100 K/min, held for 120 s and then cooled at 4 K/min to 900 °C before being rapidly cooled to room temperature.

Following in-situ observation, and after cooling to ambient temperature, the surface of each sample was examined using diffraction and spectroscopy techniques, i.e. electron backscatter diffraction (EBSD) and electron probe microanalysis (EPMA). A Zeiss Merlin field emission gun scanning electron microscope (FEG-SEM) was used for imaging studies. Back-scattered electron (BSE) and secondary electron (SE) images were collected. The SEM is equipped with a Bruker EBSD detector, which was used to capture EBSD patterns at a resolution of 600 × 800 for maps which were collected at a step size of 450 nm. A JEOL JXA-8530F Plus operating at 15 kV and 50 nA with wavelength dispersive spectrometers (WDS) was employed to perform micro-chemical composition analysis of regions on the surface. Focused ion beam (FIB) tomography was applied to study the 3D morphological features of the interfacial carbide that formed during the in-situ heat treatment. The 3D observation was performed using a JEOL JIB-4700F FIB-SEM at a sectioning condition of 30 kV and 30 nA; a carbon film was deposited to protect the field of view from FIB damage. The volume analysed was 11.7 × 14.8 × 8.2 μm^3 with a step size of 0.06 μm. BSE images were taken at 5 kV following each section. The BSE atomic number contrast allowed the differentiation of the carbide (dark) and the austenitic (γ) matrix (light), and grain boundaries could be differentiated by the electron channelling contrast. After the serial sectioning and imaging, the 3D object of interest (carbide phase) was reconstructed and rendered using Stacker NEO software [13]. Image filtering was applied to show only the 3D shape of the carbide or the carbide along with the γ (austenite) grain boundary.

The precipitation of the carbide during cooling over the range 1080 to 900 °C is illustrated in Fig. 1 with a temperature decrement of 20 K between images. See also the supplementary movie 1 that reveals the

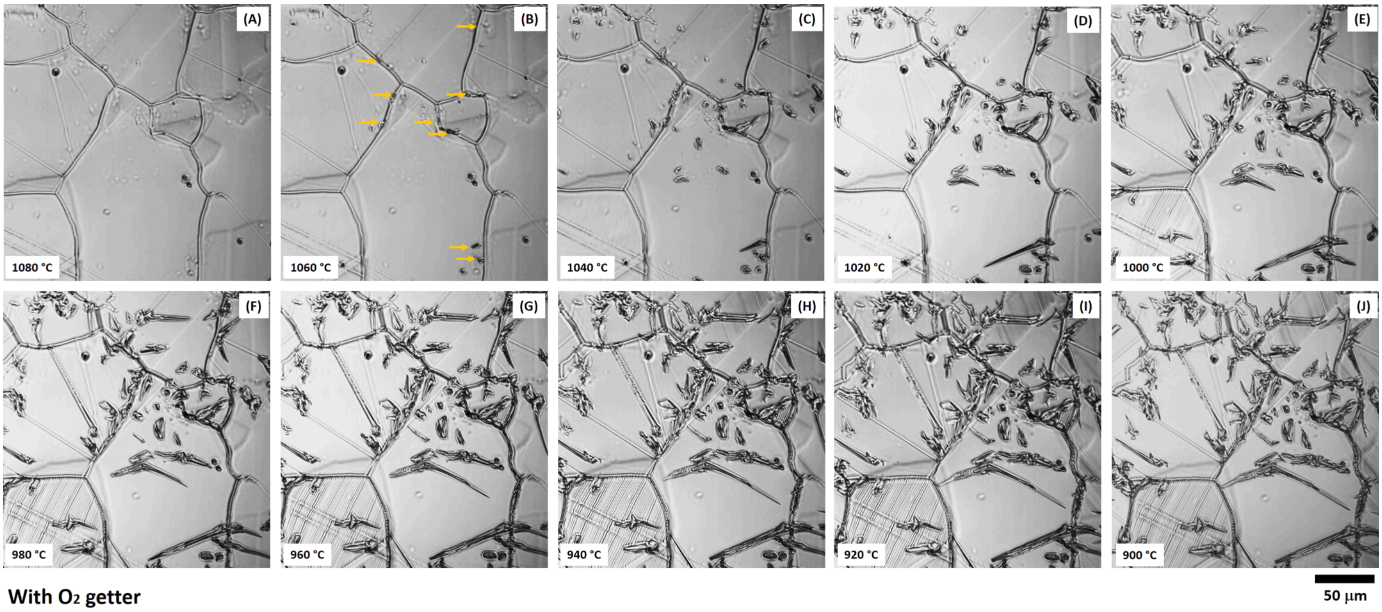

Fig. 1. In-situ observation made by HT-CLSM on the precipitation reaction of M_7C_3 carbide continuously cooled from 1080 °C to 900 °C at a 20 °C decrement. The incubation of carbide is indicated by arrows in (b). The readers are referred to supplementary video 1 for interpretation of the carbide evolution in high-definition (HD).

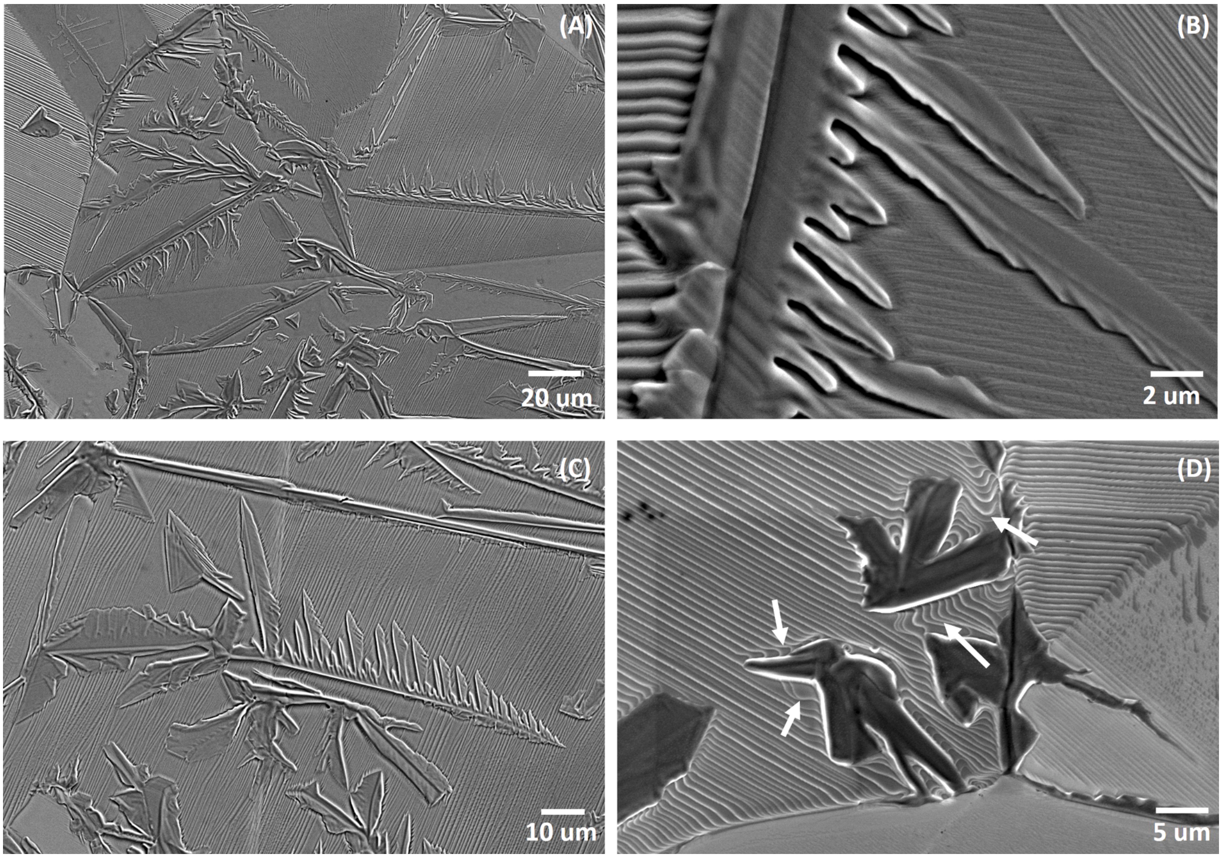

Fig. 2. Examples of solid-state dendritic growth of M_7C_3 carbide on the surface of Alloy 600 shown at different magnifications after continuous cooling, see (a–c). Distorted slip traces implies local deformation induced via carbide growth upon cooling, see pointed arrows in (d).

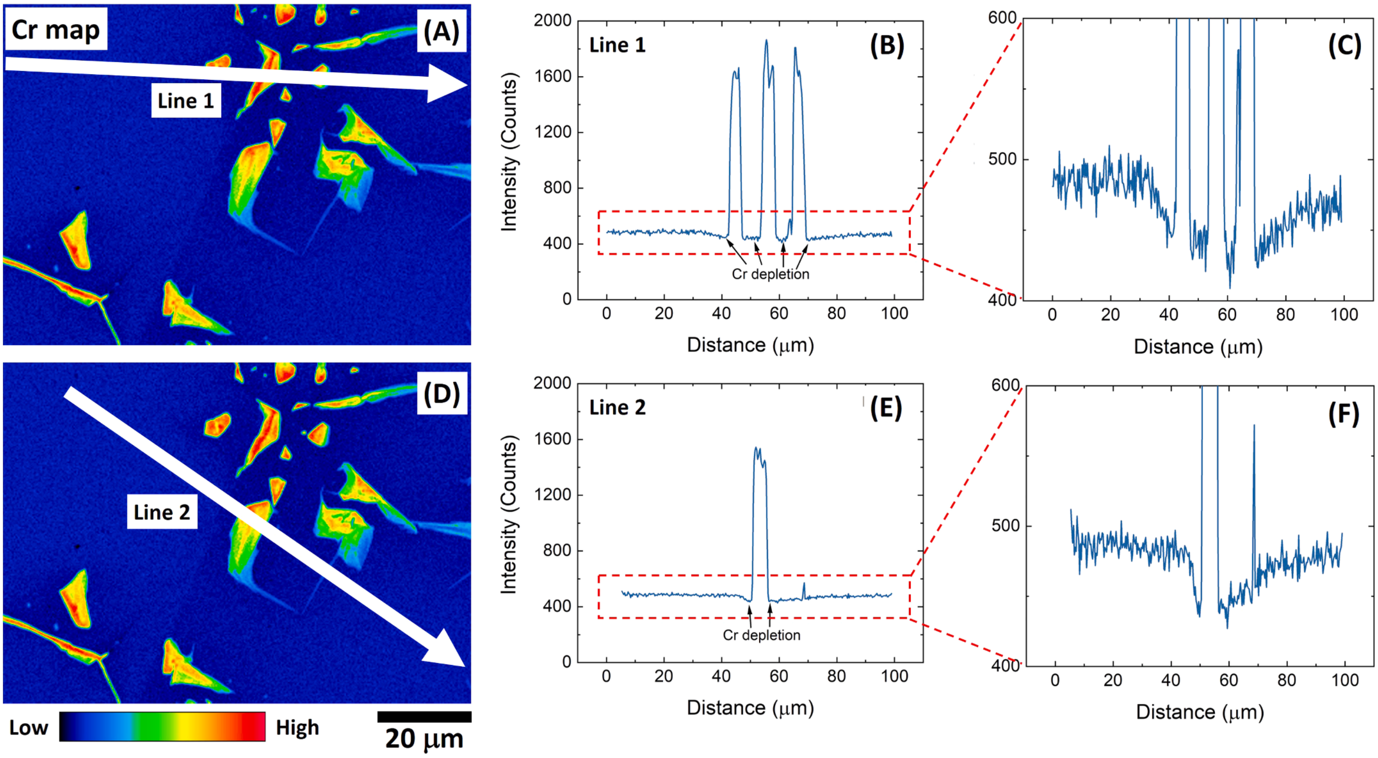

Fig. 3. Line scans from Cr-map acquired by EPMA chemical analysis. Line 1 (a–c) and line 2 demonstrate clear depletion of Cr in the vicinity of M_7C_3 carbide suggesting the growth of carbide is diffusion assisted. (For interpretation of the references to colour in this figure legend, the reader is referred to the web version of this article.)

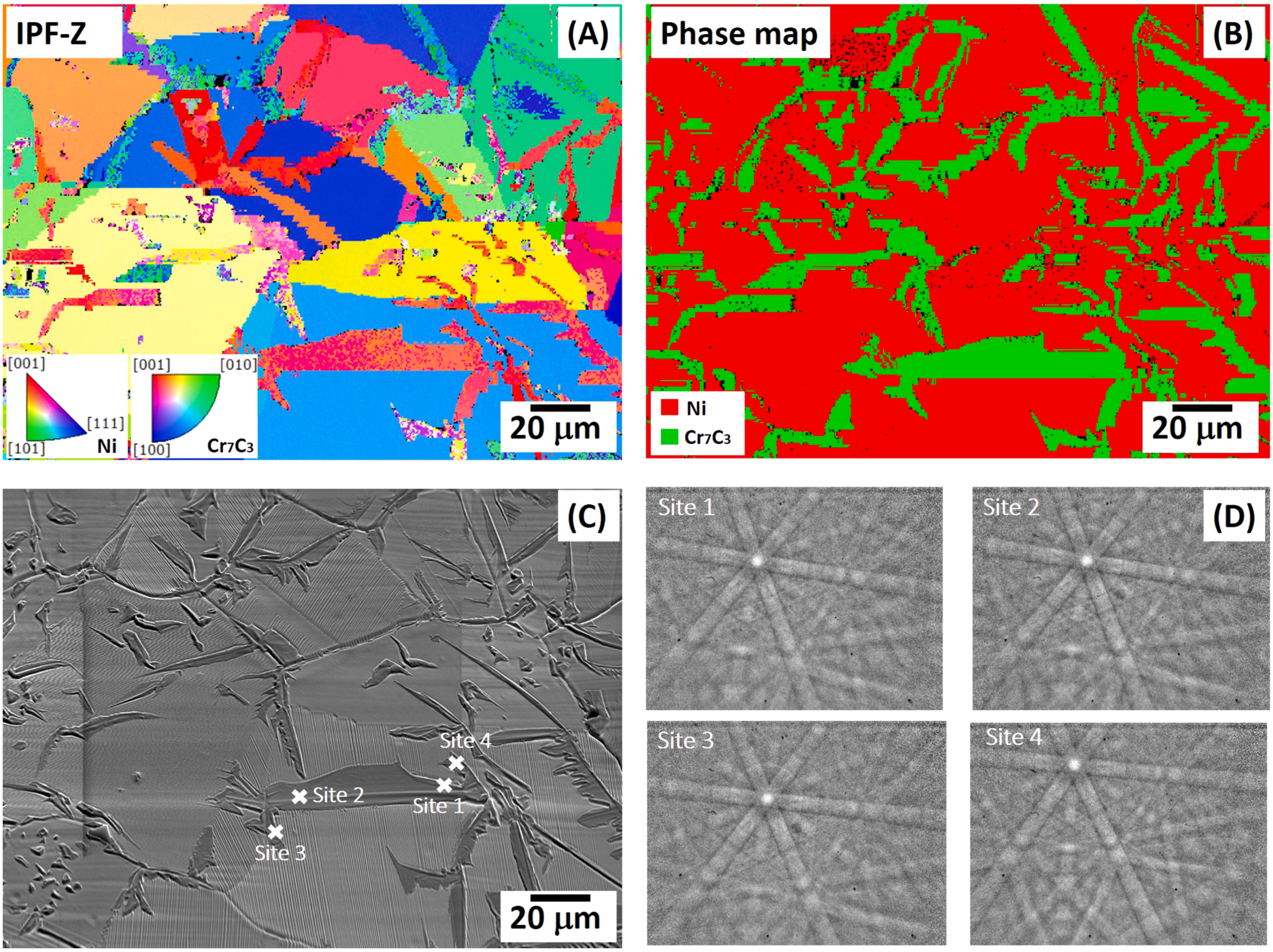

Fig. 4. High resolution EBSD characterisation of the surface M_7C_3 carbide and matrix. (a) inverse pole figure map along *Z*-axis, (b) phase map, (c) secondary electron image and (d) corresponding Kikuchi patterns from different locations of the same carbide. (For interpretation of the references to colour in this figure legend, the reader is referred to the web version of this article.)

evolution in great detail. As will be confirmed in the following section, the phase formed on the surface is M_7C_3 carbide. It is clear that the nucleation of this carbide phase is at approximately 1060 °C, which is consistent with that reported elsewhere [12]. The initial carbide nucleation site is most frequently observed to be at grain boundaries or triple junctions (see yellow arrows), for which a lower energy barrier is likely. However, with a small decrease in temperature to ~1040 °C, many other surfaces in the grain interior also have developed signs of carbide nucleation. It suggests that the energy penalty for free surface nucleation is only marginally greater than for the grain boundary, which is about 20 K of undercooling; in contrast to a more significant energy barrier for nucleation in grain interior in the bulk, where a suppression is possible [14]. Significant carbide growth on the free surface emerged whilst cooling down to ~ 960 °C, and many carbides developed with a needle-like morphology, growing to a length of over 100 μm in some cases. The growth rate of the carbide diminishes with further cooling and little noticeable change occurred below 920 °C.

The morphology of the carbide phase on the surface was characterised ex-situ, using SEM/SE imaging, see Fig. 2. The so-called “needle-like” precipitates possess a morphology that is “branched like a tree” also known as “dendrite-like”, where some precipitates display well defined secondary arms with rounded tips showing in Fig. 2(a–c). The dendrite-like phase is formed in the solid-state, in contrast to solidification from the melt, where such features are frequently seen. The secondary arm spacing is 3.0 ± 1.3 μm, averaged from 15 random precipitates. With the aid of a tilted stage, there is no notable protrusion of the carbide growing out of the free surface. Further ex-situ characterisation of carbide was achieved using chemical spectroscopy and diffraction methods. EPMA elemental maps for the elements present are shown in Figure S5; the carbide is enriched in Cr and depleted in Fe and Ni compared with the austenite matrix. Furthermore, a Cr depletion zone in the matrix, near the interface with the carbide phase, is evident from the EPMA Cr-map. Fig. 3 shows line scans of Cr intensity that confirm this observation semi-quantitatively. The Cr intensity drops relative to the background level, see arrows on the figure. The depletion of Cr near the carbide phase confirms that the mechanism of growth involves long range diffusion as has been reported from studies of bulk samples [15]. The diffusional observation during the carbide growth suggests the branched morphology of the phase transformation is facilitated by Mullins–Sekerka type instability [16]. The presence of a solute supersaturation in a matrix during continuous cooling makes the interface unstable to diffusive instability. Hence the structure observed here is distinctive to other displacive mechanisms that might result in a similar morphology, such as Widmanstätten ferrite [17].

High-resolution EBSD was also utilised to determine the crystal structure of these surface carbides. In Fig. 4(a) and (b) the carbides are identified as Cr-rich and with the orthorhombic M_7C_3 structure from the Inorganic Crystal Structure Database (ICSD) [18]. This is the same

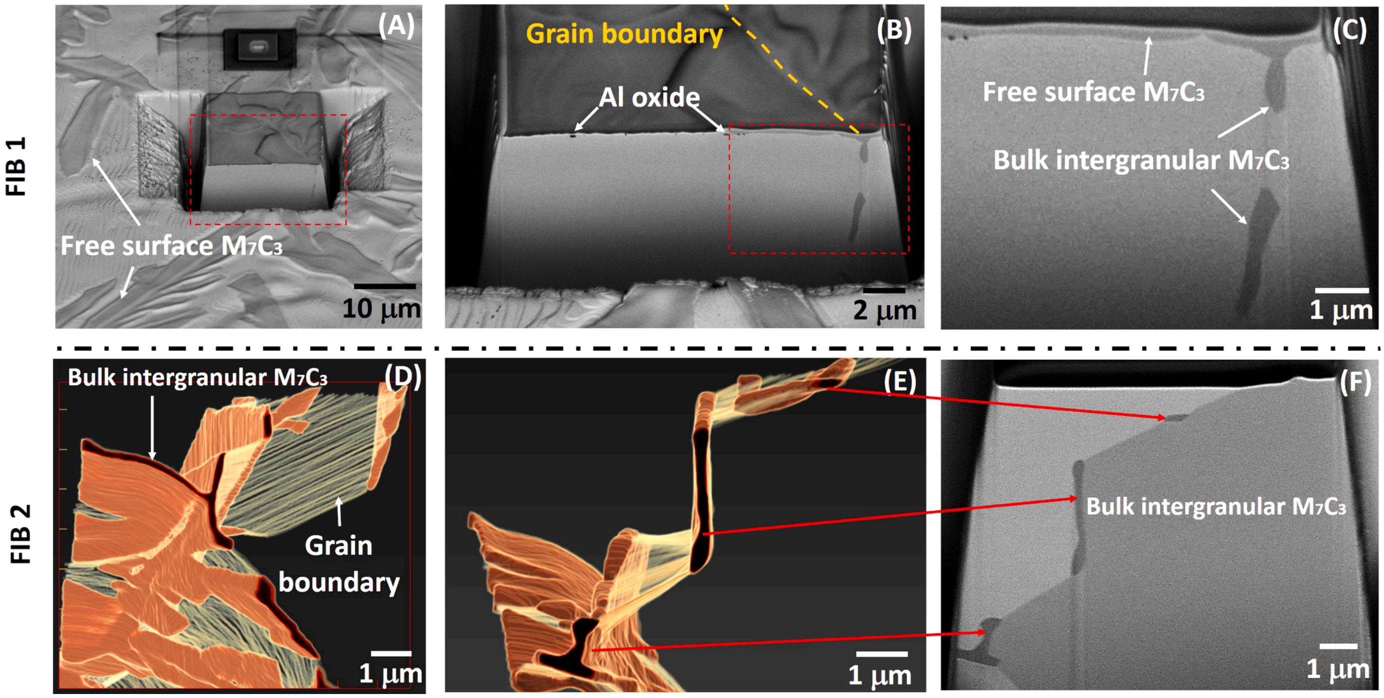

Fig. 5. 3D sectioning and reconstruction via SEM-FIB of surface M_7C_3 carbides and intergranular bulk carbides. (a–c) reveal surface M_7C_3 carbide that is physically connected to the bulk intergranular carbide. (d and e) show the reconstruction of some bulk intergranular M_7C_3 carbides from two viewing angles and (f) shows one slice of 2D cross-sectional image from which the reconstruction was derived. The readers are referred to supplementary video 2 for interpretation of the 3D carbide reconstruction.

crystal structure as the bulk grain boundary carbides previously identified in mill-annealed Alloy 600 for example by Hall and Briant [15]. Many of the surface carbides are seen to be in excess of 10 μm with branches growing in different directions. Nevertheless, EBSD Kikuchi patterns collected at locations shown in Fig. 4(c and d) confirm that different regions of a large carbide had the same orientation and thus must have originated from the same nucleus. It was also found that many, but not all, surface carbides had a $\{111\}_{\gamma}//\{100\}_{M_7C_3}$ orientation relationship with the matrix which is known to exist for bulk grain boundary M_7C_3 with one neighbouring grain in Alloy 600 [12]. The evidence is shown in the supplementary information file, Figure S6. Seven random regions of interest were selected and pole figure maps were generated which reveal the orientation relationship for M_7C_3 and the γ-matrix. Most carbides share the orientation relationships with the γ matrix to some extent, but not all. The carbides that did not display the expected relationship had grown to a such a size that the orientation relationship appears to have been lost as found previously [19]. Another possibility could be that with a sufficiently low energy barrier for nucleation at the free surface, this allows carbide nucleation without a crystallographic orientation favourable to the substrate.

It is fascinating to return to the phenomenon of the slip lines which have been found to arise during continuous cooling. This is observed to be a very general phenomenon as post-mortem examination indicates that the slip traces are distributed uniformly on the polished surfaces. Our hypothesis is that the formation of the slip lines requires a degree of oxidation of the surface – this is supported by the widespread observation of slip steps when a getter material is absent – see Figure S4 for transformation at 980 °C – but only a low density of slip lines spread when the oxygen getter is present, see Fig. 1(f). Thus, there is a probable role of the mechanical constraint arising from the formation of the oxide. In addition, since the surface will have cooled faster than the bulk, thermal gradients may also exacerbate this effect by promoting thermal stresses. Furthermore, the supplementary movie 1 demonstrates that slip lines originate at grain boundaries but few (if any) of them progress to neighbouring grains, in contrast to deformation at larger strains [20]. This implies the overall deformation on the surface is relatively small with only some grains developing signs of secondary slip during cooling to room temperature [21]. Interestingly, significant local interaction occurs between slip traces and carbides with severe slip line bending observed in their vicinity, see Fig. 2(d) as indicated by arrows. Since slip traces normally display a planar morphology akin to ‘a stack of cards’, the change in this local morphology is a manifestation of localised matrix deformation. The localised distortion of slip traces is probably caused by carbide growth and interactions between protruding carbides and/or grain boundaries. Thus, despite the material being fully annealed, the phase transformation involving carbide precipitation can cause significant volume change leading to such local deformation [12].

The surface carbides are of particular interest because of their dendritic morphology, large size and, in some cases, loss of coherency with the matrix. To establish the connection between surface and bulk intergranular carbides the FIB tomography study was undertaken. Fig. 5 (a–c) shows SEM images obtained from FIB sectioning and display a slice through a surface carbide that is connected to a bulk intergranular carbide. It is clear that the surface carbide has most likely grown from the nucleus at a grain boundary. The carbide thickness appears similar on both the free surface and at the grain boundary. Supplementary movie 2 shows clearly the reconstructued tomographic images of a grain boundary and grain boundary carbides viewed from different orientations. The largest intergranular carbide was located at a triple junction and it branched to all three orientations during growth. Reconstructed images captured from the video at different orientations are displayed in Fig. 5(d) and (e) where the dark brown corresponds to the carbide phase and the grain boundary is shown by light coloured connecting lines. The complex branched morphology of the carbide as it grew along the grain boundary is evident. This confirms that the branched dendritic growth is not confined to surface carbides but is also a feature of bulk grain boundary carbides. Finally, Fig. 5(f) is one representative BSE/SEM cross-sectional slice used to generate the 3D tomographic image. The middle carbide in contrast to the triple junction carbide, has attempted to grow into to γ-matrix. The original grain boundary has migrated accordingly to accommodate its growth.

The above observations provide important insights into interfacial carbides in Alloy 600. Despite a small number of reports which have revealed similar carbide morphology in steels and nickel [22–26], dendritic carbide growth has not been widely reported or studied. Its emergence is linked to the presence of supersaturation of the γ-matrix that results in diffusive instabilities at interfaces [27]. The frequency of occurrence of dendritic carbides following solid state precipitation is possibly underestimated as one can obtain such a structure in the present alloy, Alloy 600, simply by slow cooling from above the carbide solvus temperature. Furthermore, the possible role of dendritic carbides in affecting mechanical or corrosion behaviour (they are commonly conceived as detrimental to properties) indicates a need for further investigations [23,28]. However, recent reports have suggested that associated secondary effects with carbide formation, such as grain boundary serration can lead to an improvement of long term time dependent degradation, e.g. creep or hot corrosion [14,29]. The implications of a dendritic morphology might well allow for a deeper analyis of the effects of intergranular carbides, particularly in corrosive environment that has lacked a clear understanding for decades. Consequently, further research is required to demonstrate a quantitative relationship between the carbide development in 3D and the associated heat treatment parameters that produces it.

In summary, precipitation of orthorhombic M_7C_3 carbide was studied in-situ in Alloy 600 using HT-LSCM during continuous cooling. Its growth morphology on the surface and in the bulk have been compared using FIB-SEM tomography 3D characterisation methods. The first nucleation of Cr-rich M_7C_3 carbide occurred at ∼1060 °C followed by dendritic growth in the solid-state until ∼920 °C. The surface carbide growth was diffusion-assisted, evidenced by a depletion of Cr in the matrix near the edge of the carbide. The primary dendrites of the carbide grow and can exceed 100 μm in size, with a secondary dendrite arm spacing 3.0 ± 1.3 μm. 3D characterisation revealed that a network of carbides exists in the grain boundaries of bulk material. It is shown that surface and grain boundary carbide originate from the same nucleus. The faceted dendritic carbide precipitation also induces local deformation via coarsening where grain boundaries must accommodate their growth by migration. The frequency of occurrence of dendritic growth of carbides is believed to be underestimated in the literature. Further study on how this affects mechanical behaviour over the long term in a corrosive environment is needed due to the practical importance of stress corrosion cracking in nuclear applications.

Declaration of Competing Interest

The authors declare that they have no known competing financial interests or personal relationships that could have appeared to influence the work reported in this paper.

Acknowledgements

This work was supported by the grant for fundamental research of the Next Generation Tatara Co-Creation Centre (NEXTA), which is established with Grant-in-aid for the Promotion of Regional Industries and University from Cabinet Office, Japan.

Supplementary material

Supplementary material associated with this article can be found, in the online version, at 10.1016/j.scriptamat.2022.114585

References

[1] G.S. Was, S. Ukai, Chapter 8 - austenitic stainless steels, in: G.R. Odette, S.J. Zinkle (Eds.), Structural Alloys for Nuclear Energy Applications, Elsevier, Boston, 2019, pp. 293–347.
[2] Z. Shen, K. Arioka, S. Lozano-Perez, Corros. Sci. 132 (2018) 244–259.
[3] Z. Zhai, M.B. Toloczko, M.J. Olszta, S.M. Bruemmer, Corros. Sci. 123 (2017) 76–87.
[4] H. Coriou, L. Grall, Y. Legall, and S. Vettier. Stress corrosion cracking of Inconel in high temperature water. In Third Colloquium of Metallurgy, page 161, Saclay, 1960. North Holland. 39, 67.
[5] S. Bruemmer, L. Charlot, C.H. Jr. Corrosion, (1988).
[6] A. Aguilar, J. Albarran, H. Lopez, L. Martinez, Mater. Lett. 61 (1) (2007) 274–277.
[7] K. Weman, 19 - the weldability of steel, in: K. Weman (Ed.), Welding Processes Handbook, second ed., Woodhead Publishing, 2012, pp. 191–206.
[8] S. Lozano-Perez, J. Titchmarsh, Mater. High Temp. 20 (4) (2003) 573–579.
[9] F. Léonard. Study of Stress Corrosion Cracking of Alloy 600 in High Temperature High Pressure Water, University of Manachester, 2010. Ph.D. thesis.
[10] T.-Y. Kuo, H.-T. Lee, Mater. Sci. Eng. A 338 (1) (2002) 202–212.
[11] S. Liu, Y. Zhou, X. Xing, J. Wang, X. Ren, Q. Yang, Sci. Rep. 6 (2016) 32941.
[12] Y.T. Tang, P. Karamched, J. Liu, J.C. Haley, R.C. Reed, A.J. Wilkinson, Acta Mater. 181 (2019) 352–366.
[13] JOEL, Stack N Viz: a suite of sotware by StackerNEO and Visualizer-evo, 2-8-3 Shinsuzuharu Bldg.4F Akebono-cho Tachikawa-shi, Tokyo 190-0012, https://temography.com/.
[14] Y.T. Tang, A.J. Wilkinson, R.C. Reed, Metall. Mater. Trans. A 49 (9) (2018) 4324–4342.
[15] E.L. Hall, C.L. Briant, Metall. Mater. Trans. A 16A (1985) 1225–1236.
[16] W. Mullins, R. Sekerka, J. Appl. Phys. 35 (2) (1964) 444–451.
[17] H.K. Bhadeshia, Prevention of Hydrogen Embrittlement in Steels, ISIJ International, 2016.
[18] NIST Inorganic Crystal Structure Database, NIST Standard Reference Database Number 3, National Institute of Standards and Technology, Gaithersburg MD, 20899.
[19] I. Moore, M. Burke, E. Palmiere, Acta Mater. 119 (2016) 157–166.
[20] S. Wei, J. Kim, C.C. Tasan, Int. J. Plast. 148 (2022) 103131.
[21] N. Hansen, Metall. Trans. A 16A (1985) 2167–2190.
[22] M. Kral, G. Spanos, Scr. Mater. 36 (8) (1996) 875–882.
[23] L. Schäfer, J. Nucl. Mater. 258–263 (1998) 1336–1339.
[24] H. Li, S. Xia, B. Zhou, W. Chen, C. Hu, J. Nucl. Mater. 399 (1) (2010) 108–113.
[25] M. Ochi, R. Kawano, T. Maeda, Y. Sato, R. Teranishi, T. Hara, M. Kikuchi, K. Kaneko, Microscopy 66 (2) (2017) 89–94.
[26] X. Zhao, M. Wang, X.-C. Hao, H.-Y. Liu, X.-D. Zha, M. Gao, Y.-C. Ma, K. Liu, J. Mater. Res. Technol. 15 (2021) 3296–3309.
[27] B. Bhadak, T. Jogi, S. Bhattacharya, A. Choudhury, 2021, arXiv:2101.09964.
[28] H. Bhadeshia, R. Honeycombe, Steels: Microstructure and Properties, fourth ed., Elsevier, 2017.
[29] P. Bhuyan, S. Pradhan, R. Mitra, S. Mandal, Corros. Sci. 149 (2019) 164–177.